Journal of Volcanology and Geothermal Research 304 (2015) 253–264

Contents lists available at ScienceDirect

Journal of Volcanology and Geothermal Research

journal homepage: www.elsevier.com/locate/jvolgeores

Subsurface structure of a maar–diatreme and associated tuff ring from a high-resolution geophysical survey, Rattlesnake Crater, Arizona

Anita Marshall [a,*], Charles Connor [a], Sarah Kruse [a], Rocco Malservisi [a], Jacob Richardson [a], Leah Courtland [b], Laura Connor [a], James Wilson [a], Makan A. Karegar [a]

[a] University of South Florida School of Geosciences, 4202 East Fowler Ave, Tampa, FL 33620, United States
[b] Department of Earth-Space Physics, University of Indianapolis, 1400 East Hanna Ave, Indianapolis, IN 46227, United States

ARTICLE INFO

Article history:
Received 12 May 2015
Accepted 3 September 2015
Available online 9 September 2015

Keywords:
Phreatomagmatism
Tuff ring
Magnetic
Gravity
GPR
San Francisco Volcanic Field

ABSTRACT

Geophysical survey techniques including gravity, magnetics, and ground penetrating radar were utilized to study the diatreme and tuff ring at Rattlesnake Crater, a maar in the San Francisco Volcanic Field of northern Arizona. Significant magnetic anomalies (+1600 nT) and a positive gravity anomaly (+1.4 mGal) are associated with the maar. Joint modeling of magnetic and gravity data indicate that the diatreme that underlies Rattlesnake Crater has volume of 0.8–1 km^3, and extends to at least 800 m depth. The modeled diatreme comprises at least two zones of variable density and magnetization, including a low density, highly magnetized unit near the center of the diatreme, interpreted to be a pyroclastic unit emplaced at sufficiently high temperature and containing sufficient juvenile fraction to acquire thermal remanent magnetization. Magnetic anomalies and ground penetrating radar (GPR) imaging demonstrate that the bedded pyroclastic deposits of the tuff ring also carry high magnetization, likely produced by energetic emplacement of hot pyroclastic density currents. GPR profiles on the tuff ring reveal long (~100 m) wavelength undulations in bedding planes. Elsewhere, comparable bedforms have been interpreted as base surge deposits inflated by air entrainment from eruption column collapse. Interpretation of these geophysical data suggests that Rattlesnake Crater produced highly energetic phreatomagmatic activity that gave way to less explosive activity as the eruption progressed. The positive gravity anomaly associated with the maar crater is interpreted to be caused by coherent bodies within the diatreme and possibly lava ponding on the crater floor. These dense magnetized bodies have excess mass of $2–4 \times 10^{10}$ kg, and occupy approximately 5% of the diatreme by volume. Magnetic anomalies on the crater floor are elongate NW–SE, suggesting that the eruption may have been triggered by the interaction of ascending magma with water in fractures of this orientation. GPR imaging of the tuff ring also suggests that substantial land-slip may have occurred on the western rim, perhaps causing part of the tuff ring to collapse into the crater. Strong radar reflections indicative of well-developed weathering horizons are present as well. The techniques employed at Rattlesnake Crater demonstrate the value of combining multiple geophysical techniques in areas where exposures are limited and invasive exploration is not an option.

Introduction

Explosive phreatomagmatic volcanism creates risk for the millions of people that live within active volcanic fields around the world (Chester et al., 2000). These eruptions occur when rising magma and groundwater interact, and can produce craters 1–2 km in diameter and more than 300 m deep (Wohletz and Sheridan, 1983; Lorenz, 2003; Lorenz and Kurszlaukis, 2007; Valentine and White, 2012). The excavation of such craters, or maars, may result from one explosion or many, and the length of time between eruptions is highly variable (White and Ross, 2011). Geophysical survey methods provide valuable data about diatremes and related sub-surface features associated with maars, which greatly augment what we can observe on the surface and contribute to our understanding of the structure and eruptive mechanisms of phreatomagmatic vents (Schulz et al., 2005; Mrlina et al., 2009; Blaikie et al., 2014). Here we present new geophysical surveys and forward models of the sub-surface structure for Rattlesnake Crater, one of many phreatomagmatic eruption sites in the San Francisco Volcanic Field (SFVF) of northern Arizona, USA.

Maar craters are underlain by diatremes that contain pulverized country rock and juvenile material produced during the eruption (White and Ross, 2011; Valentine and White, 2012). The top of the diatreme is generally assumed to roughly coincide with the diameter of the surface crater, although the shape of the crater can change significantly due to syn-eruptive and post-eruptive processes such as faulting, mass wasting, subsidence, and in-filling by sediments (White and Ross, 2011). Previous geophysical surveys reveal that some maar–diatremes

* Corresponding author.
E-mail address: amarshall3@mail.usf.edu (A. Marshall).

http://dx.doi.org/10.1016/j.jvolgeores.2015.09.006
0377-0273/

have complex structures that are not evident on the surface, including multiple eruption points, igneous dikes, buried lava lakes, faults and subsidence features (Schulz et al., 2005; Mrlina et al., 2009; Blaikie et al., 2012; Bolós et al., 2012).

Surrounding the crater, a tuff ring made of ejected material forms a rim around the eruption site. Examination of the tuff ring can yield valuable information regarding magma volatile content and composition, and the duration of an eruption (Chough S.K., 1990; Sohn and Park, 2005; Brand and Clarke, 2009). Observations of erosional surfaces within tuff rings are used to infer the number of eruptive phases a vent may have produced, and the duration of repose between them (McPhie et al., 1990; Zimmer et al., 2010). Analysis of exposed deposits can also be used to estimate eruptive energy (Vazquez and Ort, 2006; van Otterloo and Cas, 2013). However, many stratigraphic studies of phreatomagmatic sites are limited by the availability of exposed units in outcrop.

Utilizing gravity and magnetic surveys is a well-established approach to studying phreatomagmatic eruption sites (Cassidy et al., 2007; López Loera et al., 2008; Mrlina et al., 2009; Bolós et al., 2012; Skácelová et al., 2012). Similarly, GPR has been widely utilized in studies of volcanic tephra and surge deposits (Russell and Stasiuk, 1997; Gómez-Ortiz et al., 2006; Gomez et al., 2008; Kruse et al., 2010; Courtland et al., 2012, 2013), and of phreatomagmatic deposits (Cagnoli and Ulrych, 2001). In this paper we use all three techniques to constrain the geometry, volume, and facies of the diatreme beneath Rattlesnake Crater and its tuff ring.

Rattlesnake Crater and the San Francisco Volcanic Field

The SFVF of northern Arizona is an active volcanic region containing more than 600 volcanic vents within 4700 km^2 (Priest et al., 2001). The SFVF is a Colorado Plateau field (Condit et al., 1989), and the locus of activity within the field has shifted from west to east with time, reflecting the motion of the North American Plate (Tanaka et al., 1986). The SFVF is bimodal, but most volcanic vents erupt basalts (Priest et al., 2001). There are at least 12 vents that show evidence of phreatomagmatic activity within the SFVF; many of these sites have complex or mixed eruptive histories.

Rattlesnake Crater is a basaltic maar and tuff ring located in the southeast region of the SFVF (Fig. 1). The crater is elongate, approximately 1.4 km in diameter on the long axis, in a NW–SE direction. The tuff ring surrounding the crater varies in height from approximately 60 m on the NE side to only a few meters high on the SW side, and is obscured on the SE side by an overlapping scoria cone, called Rattlesnake Hill. The presence of tephra from Sunset Crater (Ort et al., 2008), and the Brunes-age magnetic orientation associated with Rattlesnake Hill lavas (Tanaka et al., 1986) place the age of Rattlesnake Crater between 900 and 780,000 yBP.

Rattlesnake Crater is constructed on top of substantial lava flows, tens of meters thick that crop out in the area surrounding the tuff ring. Based on coring in the area, the sub-surface stratigraphic column comprises Paleozoic sedimentary units identified in descending order as the Kaibab, Toroweap, Coconino, Schnebly Hill, and Supai Formations (Hoffmann et al., 2006). The uppermost stratigraphic unit, the Kaibab Formation, is a fractured (Gettings and Bultman, 2005) and karsted (Montgomery and Harshbarger, 1992) Permian limestone with a maximum thickness of 200 m in the area. Underlying the Kaibab, the Toroweap Formation, a mixed variety of near-shore clastic units, is less than 100 m thick. The Coconino Sandstone, a sequence of cross-bedded fine-grained sandstone 400–500 m thick, is the primary water-bearing unit. The thin (tens of meters) Schnebly Hill Formation both interfingers with and underlies the Coconino and is made of very fine grained mudstones, limestone and dolomite units. The well logs of Hoffman et al (2006) end in the Supai Formation, sometimes grouped with a number of lower units as "Redbeds", which are a collection of distinctively colored alternating units of sandstone, siltstone and mudstone.

The entire tuff ring is covered by weathering products and fall deposits, with the important exception of a band of outcropping units

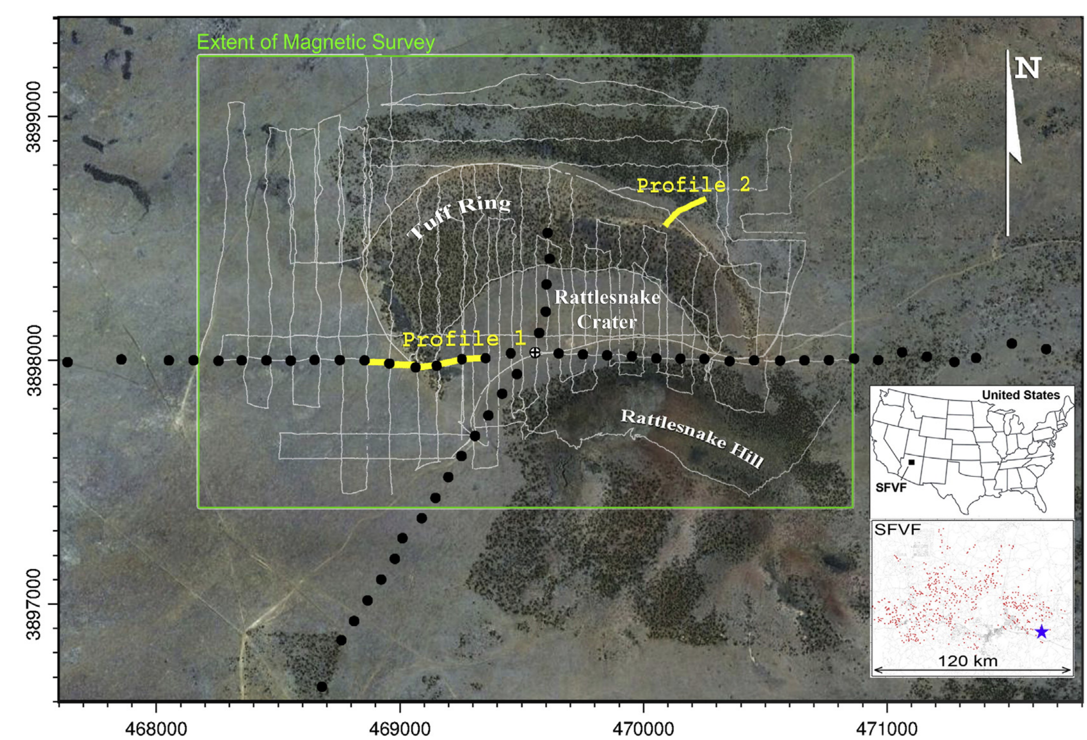

Fig. 1. Data acquisition locations for the geophysical study of the Rattlesnake Crater complex (blue star, inset), one of hundreds of volcanic vents (red dots, inset) within the SFVF, Arizona. The complex includes Rattlesnake Crater, a maar surrounded by a tuff ring and bounded to the SE by Rattlesnake Hill, a scoria cone. White lines show the track of the ground magnetic survey (Fig. 3); black dots indicate gravity survey points (Fig. 2), and yellow lines indicate the locations of GPR profiles. The green box shows the map extent of the contoured magnetic anomaly map. Map Coordinates are in UTM, zone 12. (For interpretation of the references to color in this figure legend, the reader is referred to the web version of this article.)

on the inner wall of the NE side of the crater (Fig. 1). This outcrop comprises a section of the upper ring, approximately 650 m in length, with maximum outcrop thickness of 20 m. At its widest point, the outcrop roughly follows the shape of the crater rim, then diverges downslope to the west before pinching out midway down the inside slope of the crater wall. Valentine (2012) identified a possible unconformity in the tuff ring outcrop containing basaltic fragments that may indicate the maar and the scoria cone formed concurrently, but the source of these fragments is uncertain and they may be from underlying lava flows. Xenoliths from lower Coconino and Redbed units are more abundant in the top-most layers of the tuff ring suggesting progressive deepening of explosions inside the maar diatreme (Valentine, 2012). Nevertheless, the utility of geological field mapping is limited by the lack of exposures. Furthermore, the area is protected because of the presence of archeological sites. Remnants of protected native encampments, found on both the flanks of the scoria cone and the tuff ring, rule out the possibility of trenching or similar approaches to investigate the underlying deposits in and around the crater. Gravity, magnetic and GPR surveys allow us to study the structure of the diatreme beneath the crater as well as the internal structure of the tuff ring in a noninvasive fashion.

Structural influences

Understanding structural controls on distributed volcanism is important in order to assess the potential distribution of future events, the tectonic conditions that give rise to distributed volcanism and the sequence of events during individual eruptions. Indication of structural controls can include the position of some vents on, or near, faults (Riggs and Duffield, 2008; George et al., 2015), development of vent alignments parallel or slightly oblique to fault zones (Guffanti et al., 1990; Aranda-Gómez et al., 2003), and the development of vent alignments parallel to joint sets or other tectonic fabrics (Delaney and Gartner, 1997; Nemeth et al., 2003; Cassidy and Locke, 2010; Kiyosugi et al., 2010; Re et al., 2015). There is abundant evidence in the SFVF that volcanism migrates along faults (Conway et al., 1997). Bedrock in the region surrounding Rattlesnake Crater is highly fractured, with orientations mainly to the NW and SW (Gettings and Bultman, 2005). Fractures are assumed to be the primary groundwater recharge mechanism for the Coconino Aquifer, and produce significant water yields to wells in otherwise impermeable stratigraphic units (Montgomery and Harshbarger, 1992; Hoffmann et al., 2006).

Geophysical techniques

Gravity and magnetic data can be used individually to construct models of the subsurface, but modeling both data sets simultaneously offers a better constrained and therefore more meaningful model (Schulz et al., 2005; Mrlina et al., 2009; Skácelová et al., 2012). However, models with very differing characteristics can often produce an equally good fit to the data. We present two models that produced a good fit to the observed gravity and magnetic data. Gravity anomalies often are associated with diatremes because the eruption may create density differences with the surrounding undisturbed geological section. In some cases, maar–diatremes have negative gravity anomalies resulting from the lower density of the pulverized country rock and lower-density juvenile material left in the diatreme (Schulz et al., 2005). Positive gravity anomalies result from the emplacement of a significant amount of dense material into the diatreme (Cassidy et al., 2007). In detailed ground-based surveys, an overall lower density diatreme allows subtle gravity anomalies created by subsequent intrusions and other internal structures to stand out especially well (Skácelová et al., 2012).

Magnetic anomalies associated with volcanic deposits originate from induced and remanent magnetization of intrusions, as well as the thermal magnetization of some pyroclastic deposits and lava flows (Mandeville et al., 1994; Morales et al., 2006; Fontana et al., 2011). Thermal magnetization of pyroclastic deposits surrounding the crater can be created by two different processes. Thermal Remanent Magnetization (TRM) results from hot emplacement above the Curie temperature, typically above 560 °C, but sometimes involving much lower blocking temperatures (Clement et al., 1993; Sulpizio et al., 2008). Thermal Viscous Remanent Magnetization (TVRM) involves post-emplacement magnetization due to prolonged exposure to elevated temperatures and is greatly aided by deuteric alteration, and the presence of water/steam in the subsurface (Dunlop, 1989; Hashimoto et al., 2008). Magnetic anomalies thus provide insight into a variety of emplacement mechanisms that may be active at maar–diatreme systems.

GPR radargrams are obtained by recording on a receiving antenna the return signal of an electromagnetic pulse sent into the ground from an adjacent transmitting antenna. Once emitted, this energy scatters or reflects from discontinuities in the electrical permittivity of buried features, and attenuates into the surrounding medium (e.g. Davis and Annan, 1989). As the transmitter–receiver pair is moved across the surface, the reflected signals that are returned to the receiver antenna at each position are combined to create a cross-sectional radar image of the subsurface. In volcanic deposits, strong reflections are most commonly associated with changes in moisture content, porosity, and lithology, such as those produced by buried weathering horizons (Cagnoli and Ulrych, 2001; Gomez et al., 2008; Kruse et al., 2010; Courtland et al., 2012).

Methods

Gravity data collection and processing

Fifty-seven gravity stations were occupied along two intersecting lines that cross Rattlesnake Crater: one striking West-East and the other roughly North–South. The North–South line was skewed to the west along its southern portion to avoid the steep terrain of Rattlesnake Hill. Gravity data were collected at approximately 100 m intervals except for the last two points on the ends of each line, which had 200 m spacing. Local variations in gravity over such a small area are subtle. Repeated measurements at base stations were used to correct for instrument drift. In addition to instrument drift, gravity readings were corrected to account for Earth tide, latitude, free air, and terrain (White et al., 2015). Position differences between gravity stations were measured with a total station to create a 3D network solution. Four benchmarks were tied to the global reference frame by observing the benchmark with geodetic GPS for 12 h. The coordinates of each measurement site are estimated to have vertical error on the order of +/−1 cm, which results in an error of +/−0.003 mGal.

A range of densities were used to perform Bouguer and terrain corrections on the gravity profiles and compare the results to local topography. The minimum correlation between gravity and topography was obtained using a rock density of 1900 kg m^{-3}. This value is lower than the bulk density of 1980 kg m^{-3} estimated for the Coconino Sandstone at nearby Meteor Crater (Roddy, 1978), but rock in the vicinity of Rattlesnake Crater is highly fractured (Gettings and Bultman, 2005) and some units are significantly karsted (Morgan et al., 2004), indicating a lower density is appropriate for gravity corrections at this site. Terrain corrections were made using SRTM data (Jarvis et al., 2008), with 30 m resolution. The resulting profiles were de-trended to remove the regional gravity gradient.

Magnetic data collection and processing

Magnetic surveys were conducted during two separate trips to obtain coverage of the entire volcano (Fig. 1). Each survey was conducted on foot using a cesium-vapor magnetometer. Data were collected by teams of two: a leader with a handheld GPS for navigation and a person following with the magnetometer and a GPS data logger. N–S survey lines were spaced 50 m apart inside the crater and every 100–200 m outside the crater. E–W lines were collected on the northern side of the tuff ring where terrain allowed, roughly 150–200 m apart. Magnetic data were not collected on the steepest parts of the tuff ring or on the slopes of Rattlesnake Hill. Along collection lines, sample spacing is approximately 1 m, and a total of 72,437 magnetic measurements were collected.

The positions of magnetic readings were retrieved by matching the time stamp records of the magnetometer and GPS data logger. Sensor dropouts and spikes in the data were removed by setting a maximum allowable change in neighboring magnetic readings (1 m apart) to <80 nT, and removing points that create a slope greater than 80 nT/m from the dataset (George et al., 2015). The regional total magnetic field strength, based on the international geomagnetic reference field (IGRF), was subtracted from each day's data before combining with other survey results.

After processing, data reproducibility was assessed by comparing all line crossings. Line crossings were defined as magnetic readings taken less than 5 m apart on the ground and separated by more than 30 min in time (George et al., 2015). The mean difference among the line crossings in our survey is 0.48 nT with a standard deviation of 167 nT. The standard deviation of 167 nT is a result of very high localized magnetic gradients within the survey area, produced by bombs and blocks buried in the shallow subsurface. As expected, we found that line crossing errors were greater on steeper terrain, probably due to the position of the sensor with respect to the slope. We note that survey error, expressed as the standard deviation at crossing points, is <10% of the total magnetic data range.

The magnetic map was filtered by upward continuation to aid in interpretation of magnetic anomalies. This technique uses a mathematical filter to attenuate the influence of shorter wavelength anomalies. In effect, this results in a magnetic map that appears as it would if the data had been collected using a sensor located at greater height above the topographic surface. Data from the first survey was upwardly continued 2 m before being combined with data from the later survey to account for a difference in sensor heights between the two surveys. The combined data was then interpolated to a grid with 10 m spacing. Two upward continuations were performed. A 5 m continuation shows the data with all but the very shortest wavelength anomalies, which are typically caused by surface noise such as individual pyroclasts. A 50 m continuation produces a map that illustrates anomalies with wavelengths typically associated with material tens of meters below the surface.

GPR data collection and processing

Two GPR profiles were collected on the tuff ring surrounding Rattlesnake Crater (Fig. 1). Profile 1 extends 500 m over the west side of the tuff ring and part of the crater floor on the shorter, more gently sloping side of the tuff ring where there are no outcrops. The data were acquired with 50 MHz unshielded antennae spaced 2 m apart and moved by manually repositioning the antennae every meter along the survey line. Profile 2 traverses 325 m of the outer slope of the taller, steeper side of the tuff ring and was acquired with a 250 MHz shielded antenna pair pulled on a sled.

GPR survey conditions were cool and dry, with no recent rainfall. Data were processed with the software package ReflexW using a dewow filter, time zero adjustments, and uniform linear gain adjustments. Profile 1 was migrated with a uniform velocity diffraction stack migration. The profiles were then corrected for topography. Analysis of diffraction hyperbolas indicates the radar velocity was approximately 0.13 m/ns and relatively uniform along both profiles over the 0.3–10 m depths of the reflecting horizons. This velocity was used to migrate the 50 MHz data, to convert time to depths, and to correct for topography.

At the 0.13 m/ns velocity, the center frequency of the 50 MHz pulse corresponds to a wavelength of ~2.6 m; that of the 250 MHz pulse to ~50 cm. Thus the radar wavelengths are longer than the thickness of most individual beds observed in the tuff outcrop. Vertical resolution can be characterized as approximately one fourth of the radar wavelength (Guha et al., 2005). Thus, horizons in a radargram will capture the attitude of beds, but there may not be a one-to-one correspondence between radargram returns and subsurface contacts. Lower frequency antennae, like the 50 MHz used to collect Profile 1, provide greater depth penetration, but lower spatial resolution. Conversely, the 250 MHz antennae used to collect Profile 2 provides finer spatial resolution, but with much less penetration into the subsurface.

Geophysical anomalies and their interpretation

Gravity anomalies

An overall positive gravity anomaly was detected within Rattlesnake Crater. The gravity data have an overall range of 1.4 mGal with maximum positive amplitude near the center of each profile line. The positive anomaly extends over the entire crater on the W–E profile line and over a portion of the crater in the S–N direction (Fig. 2). This positive anomaly is the result of denser material in the subsurface in the crater area relative to the undisturbed section outside the crater. On the W–E profile, a significant gravity low (−0.7 mGal) correlates with the location of the tephra ring on the E side of the crater. The elevated gravity readings just outside the tephra ring on both sides of the crater on the W–E profile coincide with lava flows surrounding the crater. On the S–N profile, the highest gravity readings are near the center of the crater, and drop off sharply on the N end of the crater. The low gravity readings at the N end of the S–N profile may be a result of the low density material in the tephra ring. A low related to the tephra ring on the west side of the crater may be masked by the proximity of lava flows from Rattlesnake Hill. Our attempts to collect gravity measurements on the north side of the tephra ring, which is steep and densely vegetated, were not successful, so the S–N measurements do not continue past the crater to the north. There is no tephra ring exposed on the southern end of the S–N profile; the gravity signature on the southern end is a result of traversing deposits from Rattlesnake Hill.

Magnetic anomalies

The magnetic map (Fig. 3) reveals anomalies associated with mapped features, and others that do not correspond with features visible on the surface, which are interpreted to be the result of sub-surface structures. The primary positive anomaly in the center of the map corresponds to the crater and has an area of about 0.48 km^2 (Fig. 3, Letter A). The highest amplitude region inside this central anomaly (+1600 nT) is elongate NW–SE, parallel to the long-axis of the maar. The strongly positive magnetic anomaly to the south of the crater corresponds to spatter on the summit rim of Rattlesnake Hill (Fig. 3, Letter B). In the SW quadrant of the map, a band of positive anomalies extends to the edge of the survey area, and has no corresponding surface feature (Fig. 3, Letter C). On the west side of the map, a mottled pattern of weaker anomalies cover the area between the tuff ring and the edge of the survey map (Fig. 3, Letter D). Wrapped around the central crater anomaly, a roughly horseshoe-shaped positive anomaly corresponds to the tuff ring (Fig. 3, Letter E). Along the SW section of the tuff ring, anomalies E and C become difficult to distinguish from one another. The trend of negative readings in the northern part of the map generally follows the pattern expected for the dipole signature of normally magnetized material in the northern hemisphere. The trend is even more apparent on the 50-m upward continuation of the magnetic anomaly map (Fig. 4).

The magnetic anomaly marked as Feature A in Figs. 3 and 4, paired with the coincident positive gravity anomaly (Fig. 2) indicates the presence of dense, highly magnetized material within the diatreme. Feature A is within the map area of the crater, with the exception of the NW section. In the NW, the anomaly extends beneath the base of the inner

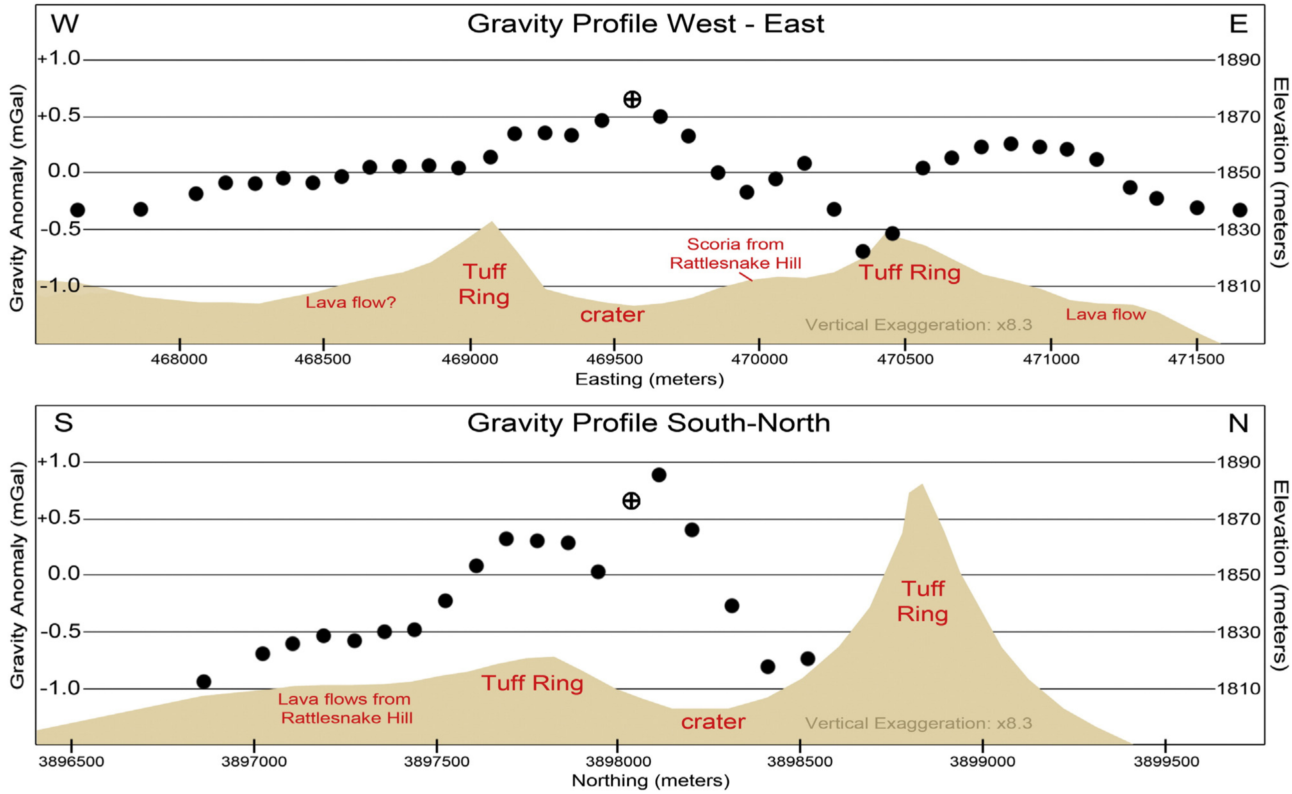

Fig. 2. W–E (top) and S–N (bottom) gravity profiles crossing Rattlesnake Crater. Solid black circles show the complete Bouguer gravity anomaly (mGal); circle with + symbol shows gravity measurement at a single shared point between the two profiles. The brown-shaded area shows topographic elevation (m) measured by total station and GPS during the survey. See survey map (Fig. 1) for point locations. (For interpretation of the references to color in this figure legend, the reader is referred to the web version of this article.)

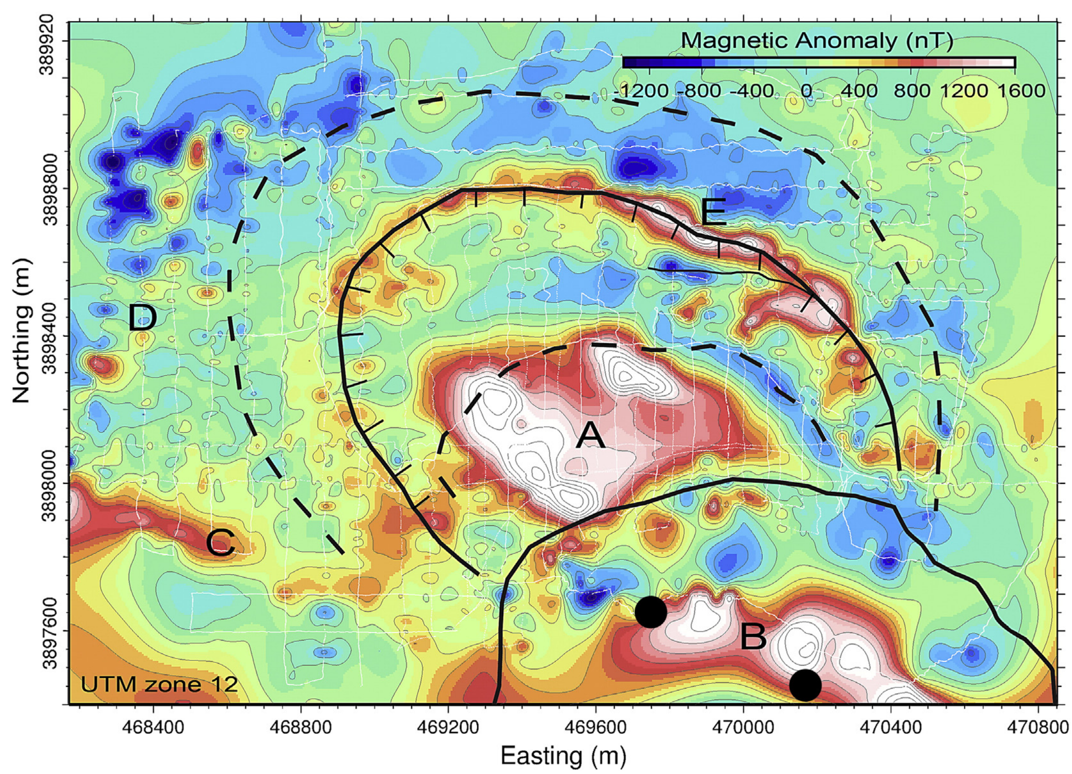

Fig. 3. Magnetic anomaly map of Rattlesnake Crater and surrounding area. Magnetic data (thin white lines; see also Fig. 1) were interpolated to a grid and filtered by upward continuation to 5 m. The geologic sketch (in black) shows the tuff ring rim (solid line with cleats), break in slope at the base of the tuff ring (dashed line) and the trace of the top-most exposure of the outcropping section (thin line on the inside rim just below the Label E).The solid outline to the southeast of the tuff ring is the break in slope at the base of Rattlesnake Hill, black dots are Rattlesnake Hill vent locations. A third vent outside the map boundaries is not shown. Areas of interest include: A, the primary anomaly beneath Rattlesnake Crater, B—the rim of Rattlesnake Hill, C—a linear anomaly with no surface expression, D—a region of mottled short wavelength anomalies, E—the anomaly associated with the tuff ring.

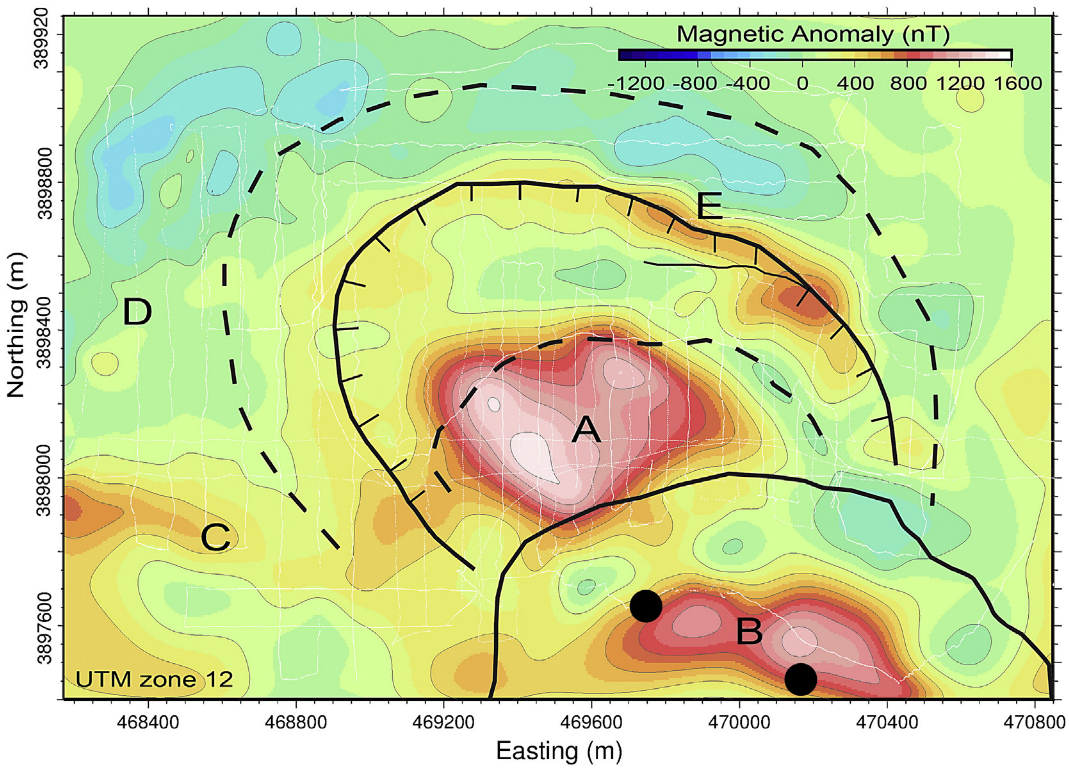

Fig. 4. Magnetic anomaly map of Rattlesnake Crater, filtered by upward continuation to 50 m to highlight comparatively long wavelength anomalies, likely associated with more prominent volcanic features. Letters are the same as those used in Fig. 3: A, the primary anomaly beneath Rattlesnake Crater, B—the rim of Rattlesnake Hill, C—a linear anomaly with no surface expression, D—a region of mottled short wavelength anomalies which are not visible at this higher continuation, E—the anomaly associated with the tuff ring.

debris apron of the tuff ring. Morphologically, the shape of the tuff ring is broader and less steep at this location compared to the rest of the tuff ring. It may be that the inner wall of the western section of the tuff ring has collapsed, shifting material from the wall further into the crater on the NW side. This could also explain why the outcropping unit on the NE section of the inner wall (drawn on Figs. 3 & 4 just below the letter E) is not present in outcrop on the NW side. Feature A is modeled as an intrusion (or intrusions) within the diatreme and a shallowly-buried lava flow within the crater (Fig. 5).

The large anomaly SE of the crater represents the positively magnetized material of Rattlesnake Hill (Figs. 3 & 4, Letter B). Our survey of Rattlesnake Hill was limited by topography to the lower flanks and one transect across the top, so the anomaly shown is an incomplete representation of the magnetic signature of the volcano.

A nearly continuous band of positive magnetic values west of Rattlesnake Hill can be seen on both versions of the magnetic map (Figs. 3 & 4, Feature C). Feature C most likely represents a lava flow. Its strong signature in the 5 m upward continuation (Fig. 3) indicates the top of the flow must be relatively close to the surface. It is also evident on the 50 m continuation (Fig. 4), so the flow must be relatively thick; at least tens of meters. A nearby outcropping lava flow, assumed to be from Rattlesnake Hill, has a measured thickness of 21 m (Harburger, 2014). Other basaltic flows in the SFVF have measured thicknesses of more than 30 m (Harburger, 2014), so a flow tens of meters thick is plausible. This lava flow is not evident on the surface by outcrop or topography, but may be part of a flow that outcrops on the west side of Rattlesnake Hill.

An area of mottled, short-wavelength anomalies extends along the west side of the survey area (Fig. 3, Feature D). Some of these anomalies correlate to small lava outcrops on the side and near the base of the tuff ring. These anomalies strongly attenuate as a result of 50 m upward continuation (Fig. 4), suggesting they result from very shallow bodies, most likely just beneath the surface. Field observations were inconclusive in determining the stratigraphic relationship between this lava flow and the tuff ring. These small lava outcrops could be clastogenic in origin, relating to an episode of fountaining, or these flows may come from a buried vent beneath the tuff ring, as small buried vents have been documented under maar deposits at other phreatomagmatic sites in the SFVF (Valentine, 2012). Alternatively, this flow may connect to the flow marked as Feature C to the south (Fig. 3), though there are substantial differences in the amplitude and wavelength of these anomalies in the magnetic data.

The entire rim of the tuff ring has a positive magnetic signature (Figs. 3 & 4, Feature E). The highest amplitude magnetic anomalies are on the NE section and coincide with the tallest part of the ring. Many tuff rings have little to no magnetic signature due to the random orientation of pyroclasts deposited below the Curie temperature. There are two possible explanations for the magnetic signature of the tuff ring. One possibility is that at some point during the eruptive history, magmatic eruptive activity deposited spatter or some other basaltic material around the crater. This is the case at other phreatomagmatic vents in the SFVF such as Colton Crater and Red Mountain (van Kooten and Buseck, 1978; Riggs and Duffield, 2008). The other possible explanation is that the magnetic signature is from the pyroclastic material which makes up the tuff ring itself. Tephra packages emplaced rapidly and in sufficient thickness could maintain enough heat after deposition to produce significant TRM. The positive magnetic signature of the tuff ring is inferred to be strongest along the rim because the inner and outer slopes of have undergone significant weathering. Slope failure could also cause a random orientation to the magnetically oriented clasts.

Gravity and magnetic modeling

Model properties

Gravity data and magnetic data collected along the E–W gravity profile were used to create two forward models of the maar–diatreme.

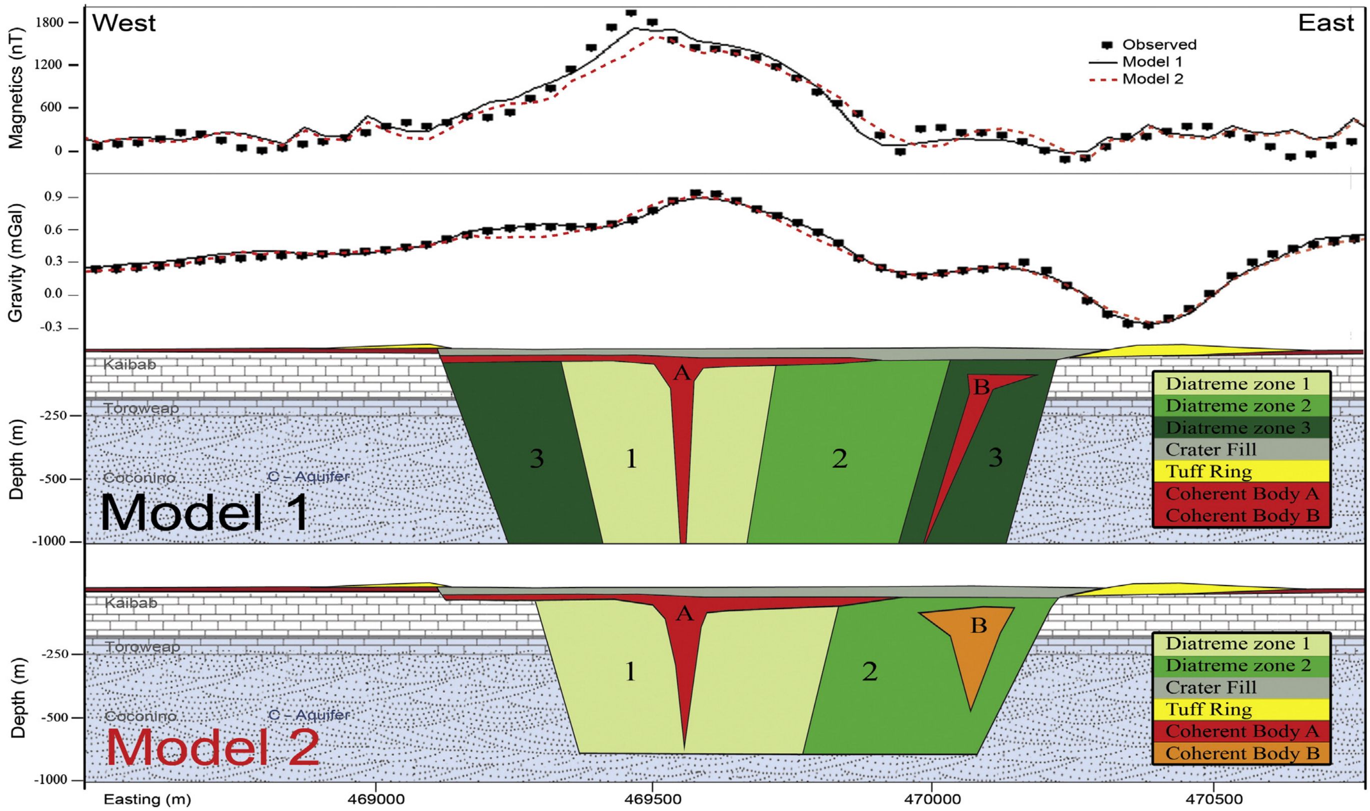

Fig. 5. 2 ¾ D geophysical models of the diatreme with magnetic and gravity data. The models were created along the West–East gravity survey line which extends across the boxed area shown on Fig. 1. Density and susceptibility values for modeled bodies are listed in Tables 1 and 2, color code shown in inset boxes. Figure shows the only the upper 1000 m of Model 1 for ease of comparison to Model 2. The distance across the profile is approximately 2.2 km. Anomalies are modeled to extend 0.7 km perpendicular to the profile in both directions. (For interpretation of the references to color in this figure legend, the reader is referred to the web version of this article.)

Magnetic data were modeled as the apparent magnetization resulting from thermally magnetized diatreme fill and tuff deposits, remanent magnetization of intrusions within the diatreme, and lava flows near the surface (Fig. 5).

Forward models were created using OASIS Montaj and Gm-Sys software packages. These programs allow the user to create model geometries of the sub-surface, assign values for density and magnetic susceptibility, and compare the resulting calculated gravity and magnetic anomalies with observed data. Our model was created using a 2 ¾ D approach as outlined in the GMSYS user's manual (Popowski et al., 2009). A 2 ¾ D model allows the user to specify how far each object extends into and out of the plane of the profile line, and also allows those objects to intersect the profile line at an angle other than 90°. The area beyond the edges of these defined shapes can only have one set of attributes. This area is designated in our models as “Country Rock”, and set to 1900 kg m^{-3} density and zero magnetic susceptibility. For simplicity and ease of comparison, all model objects inside the diatreme were specified to extend 0.7 km into and out of the plane of the model profile, perpendicular to the profile, for a total width of 1.4 km. We note that model results are only marginally sensitive to the width of these modeled objects, within reason constrained by the outcrop pattern of the crater and tuff ring. Stratigraphic and aquifer depth information shown on the model (Fig. 5) are derived from a well drilled roughly 20 km W of our study site (Hoffmann et al., 2006). The depths and thicknesses of units are approximations, as depth and stratigraphic characteristics may vary over relatively small distances.

Our magnetic calculations are based on apparent magnetization, a combination of induced and remanent magnetization described by:

$$k_{apparent} = T/H \tag{1}$$

where T is the magnitude of the total vector of magnetization, and H is the magnitude of the Earth's magnetic field.

$$T = kH + J_r \tag{2}$$

where k is the magnetic susceptibility, and J_r the magnitude of the vector of remanent magnetization. This estimate assumes that the vector of remanent magnetization is parallel to the current direction of the Earth's field, H, which is a reasonable assumption for the normally magnetized Rattlesnake Crater anomalies.

Model #1:

The modeled diatreme has the same density as the surrounding country rock, with the exception of its innermost zone. The primary magnetic and gravity anomaly within the crater is modeled as a single body of relatively high magnetization and high density (2500 kg m^{-3} and 0.037 SI respectively), consistent with coherent basalt (Fig. 5, Coherent Body A). The thin vertical segment tapers out at a depth of approximately 1 km, although this depth is not especially well constrained. The vertical portion of Coherent Body A is topped by a thin horizontal body of similar density and magnetization which extends approximately 800 m along the profile line. This horizontal body either represents a lava flow deposited on the paleo-crater floor and buried by subsequent deposits, or a shallow sill within the diatreme. Coherent Body B is given the same density and apparent susceptibility, and also assumed to be a basaltic intrusion in this model. The diatreme is divided into zones of inwardly increasing apparent magnetic susceptibilities (0.013, 0.025, and 0.063 SI) and decreasing densities (1900 kg m^{-3} and 1800 kg m^{-3}) similar to the approach of Mrlina et al. (2009) (Table 1). The tuff ring surrounding the crater was modeled

Table 1
Density and susceptibility values used in Model #1 (Fig. 5).

Model components	Density (kg/m^3)	Apparent susceptibility, SI
Country rock	1900	0.000
Diatreme zone 1	1800	0.062
Diatreme zone 2	1900	0.025
Diatreme zone 3	1900	0.013
Crater fill	1850	0.000
Tuff ring	1700	0.037
Coherent body A & B and surface lava flows	2500	0.188

with a density of 1700 kg m^{-3} and an apparent susceptibility of 0.037 SI. The top layer of fill in the crater was modeled as 1850 kg m^{-3} with zero magnetic susceptibility.

Model 1 indicates a dip-angle of 79°–83° for the inwardly-dipping diatreme walls. Along the E–W profile line, the diameter of the top of the diatreme is approximately 1.1 km, roughly the same width as the distance across the crater floor along the profile. The diatreme is not modeled below a depth of 1500 m, as the model is not sensitive to reasonable changes in density and susceptibility below that depth. If we assume an inverted cone-shaped diatreme, with inwardly dipping walls of 80°, the maximum depth of the modeled base of the diatreme is about 3 km in Model 1. This depth is consistent with Valentine's depth estimate based on the xenolith content of the tuff ring (Valentine, 2012). Using this depth and the inverted cone geometry yields a maximum diatreme volume of approximately 1 km^3. If instead that same cone is truncated at 1500 m, the maximum depth to which we modeled the diatreme, the diatreme volume is approximately 0.9 km^3. Based on these calculations, the volume of the diatreme beneath Rattlesnake Crater is approximately 0.9–1 km^3.

Model #2:

The diatreme in Model 2 extends to a depth of ~800 m, and maintains the dip angle on the outer walls of the diatreme of about 80°. As in Model 1, the primary magnetic and gravity anomaly within the crater (Fig. 5, Coherent Body A) is modeled as a single body of relatively high magnetization and high density; although the density is lowered from 2500 to 2400 kg m^{-3}, and the vertical portion of the body tapers out at a depth of 0.5 km. The horizontal component remains nearly identical in its geometry to Model 1. Coherent Body B is significantly different in its geometry, as well as having a lower modeled density of 2300 kg m^{-3} and a much lower apparent susceptibility of 0.088 SI. While the susceptibility and density values assigned to this body in Model 2 are much lower that they were in Model 1, they are still significantly higher values than the surrounding diatreme. The higher magnetization and density indicates that Body B is likely some sort of coherent material, that is of uniform density and magnetic properties, although not of the same density or apparent magnetic susceptibility as Body A. Body B may represent a deposit like spatter (e.g. Lefebvre et al., 2012), which would have a lower density and lower susceptibility than a lava flow or sill, but still significantly higher values than the surrounding diatreme.

Table 2
Density and susceptibility values used in Model #2 (Fig. 5).

Model components	Density (kg/m^3)	Apparent susceptibility, SI
Country rock	1900	0.000
Diatreme zone 1	1850	0.050
Diatreme zone 2	1880	0.013
Crater fill	1800	0.000
Tuff ring	1700	0.037
Coherent body A	2400	0.188
Coherent body B	2300	0.088

In Model 2, the density of the top layer of fill in the crater is lowered from 1850 kg m^{-3} to 1800 kg m^{-3}, while the magnetic susceptibility of the fill remains at zero. The diatreme is simplified into two zones, and the outer zones, which in Model 1 were only delineated from the country rock by a small apparent magnetic susceptibility, are eliminated. In contrast to Model 1, the entire diatreme in Model 2, excluding the coherent bodies, has a lower density than the surrounding country rock: 1850 kg m^{-3} and 0.050 SI for Zone 1; and 1880 kg m^{-3} and 0.013 SI for Zone 2 (Table 2). Diatreme Zone 1 was given a significantly higher magnetization than in Model 1. This higher magnetization is required to make up for the response that was a result of the deeper diatreme and longer vertical component of Coherent Body A in Model 1. Because Diatreme Zone 3 in Model 1 was distinguished from the country rock only by a slight magnetic susceptibility, Zone 3 can be removed from the left side of the diatreme without a change in fit to the observed data. Body A has such a strong control on the magnetic response of this section of the model that the small contribution to the overall magnetic signal from the diatreme is negligible.

Model similarities:

In Models 1 and 2, Coherent Body A was modeled as tapering out at depth (1 and 0.5 km respectively) and topped by a thin horizontal body of similar density and magnetization. The depth to the horizontal body is 30–40 m beneath the current crater floor. In both models, the central positive gravity anomaly is due almost entirely to the presence of this relatively dense magnetized body. Assuming that the gravity anomaly measured along the profile is axisymmetric, we use Gauss' law to estimate the total excess mass producing the gravity anomalies of Body A and Body B to be approximately 4×10^{10} kg for Model 1. Given the density contrast between the intrusion and the diatreme fill of approximately 700 kg m^{-3} in Model 1 (Table 1), this yields a volume of the coherent body of approximately 0.06 km^3. Therefore, approximately 7% of the diatreme volume consists of coherent material in Model 1. The density contrast in Model 2 is lower, approximately 500 kg m^{-3}, and the modeled diatreme is shallower than Model 1. Using the same approach for making the calculations, the coherent bodies in Model 2 have a total volume of approximately 0.03 km^3, and make up roughly 5% of the diatreme. In both models, fitting the observed gravity and magnetic data requires that Diatreme Zone 1 have higher magnetization and lower density than the other zones of the diatreme. This change can be explained by an increase in the fraction of pulverized material and hotter emplacement in Zone 1 compared to the outer zones where lower-temperature emplacement occurred. The slightly higher density in the outer zones of the diatreme may also be the result of a significant portion of wall rock being incorporated in the outer sections of the diatreme.

The elevated magnetic readings and low gravity readings associated with the tuff ring are accounted for by modeling the tuff ring with a density of 1700 kg m^{-3} and an apparent magnetic susceptibility of 0.037 SI in both models. This supports the idea that the positive magnetic values of the tuff ring are a result of TRM of pyroclastic deposits rather than buried deposits of denser magnetized material.

GPR

GPR Profile 1 (Fig. 6) extends over the peak of the tuff ring and down onto the crater floor with a maximum penetration depth of about 20 m. Several notable features lend insight into the structure of this phreatomagmatic system. On the outside of the tuff ring, parallel beds dip approximately 15° away from the crater (Fig. 6, Feature 1). These reflectors continue past the depth of signal penetration (10–15 m) and are interpreted as surge deposits. (e.g. Sohn and Chough, 1989; Chough S.K., 1990; White, 1991; Vazquez and Ort, 2006; Ort and Carrasco-Núñez, 2009). These deposits dip relatively uniformly along

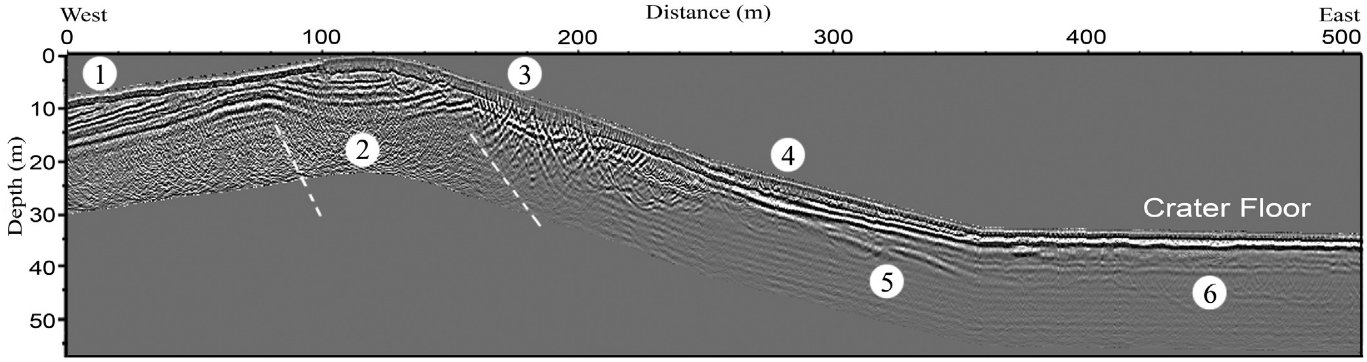

Fig. 6. Profile 1–50 MHz profile over the west side of the tuff ring (see Fig. 1 for location). The profile shows the data corrected for topography with time converted to depth assuming a uniform velocity of 0.13 m/ns. White dashed lines indicate inferred fault locations. Numbers mark features discussed in text.

the ~100 m of the profile beyond the rim. If these outward-dipping beds are part of a larger waveform, the wavelength must be >~250 m.

Beneath the crest of the tuff ring, reflectors to a depth of ~12 m form a very gentle trough filled with progressively slightly flatter layers (Fig. 6, Feature 2). One possible explanation is that gravity-driven faulting within the tuff ring, beneath the site of the current rim, created accommodation space. The trough progressively shoaled and flattened as successive deposits in-filled. Fall deposits from later eruptions may contribute to the trough fill. Alternatively, this feature may be part of a longer-wavelength depositional bedform. Brand and Clarke (2009) compile wavelengths of surge deposit bedforms as a function of distance from the vent for 7 sites. Of these, the Rattlesnake western rim feature (~100 m wavelength; ~600 m from vent) fits most closely with a series of depositional packages documented at the phreatomagmatic Table Rock Complex in Oregon (Brand and Clarke, 2012, Fig. 2e). At the Table Rock Complex, the long wavelengths are interpreted as the product of super-critical flow conditions (Brand and Clarke, 2009) in which inflated base surge deposits can scour underlying material.

On the inside slope of the tuff ring, a trough of surficial sediments up to 5 m thick covers features that strongly diffract the GPR signal (Fig. 6, Feature 3). The U-shaped features on the radargram near Feature 3 are an artifact of imperfect collapse of diffractors in the 2D migration of the data. We interpret these diffractors as the shallow termini of beds that have been truncated by erosion or slope failure on the inner face of the tuff ring. Similar truncation surfaces have been observed in outcrop at other tuff ring locations (Sohn and Park, 2005; Brand and Clarke, 2009, 2012). Another trough filled with surficial sediments lower on the slope (Fig. 6, Feature 4) is most likely the result of grain avalanching. Towards the bottom of the tuff ring (Fig. 6, Feature 5), a set of buried reflective horizons overlap each other and dip towards the crater. These could represent on-lap deposits from successive surges within the crater.

There are horizontal reflectors to about 8 m deep beneath the crater floor (Fig. 6, Feature 6). These are the result of post-eruptive fill layers and/or soil horizons. Deeper reflectors within the crater cannot be interpreted reliably due to high attenuation within the crater. We suspect this higher degree of attenuation is related to soil development on the crater floor.

GPR Profile 2 (Fig. 7) is a 250 MHz survey line collected on the eastern side of the tuff ring. The profile starts at the crest and continues east, away from the crater, and down the outer slope of the tuff ring. The units beneath the crest of the tuff ring (Fig. 7, Feature 1) are not roughly horizontal, as they are on GPR Profile 1, but dip steeply (approximately 50°) away from the crater. This difference highlights the variable nature of the depositional and/or post-depositional processes affecting the tuff ring.

Downslope from the crest, the reflecting units exhibit symmetrical wave-like features (Fig. 7, Feature 2) with wavelengths of ~100 m, and amplitudes of ~5–8 m. The depth of penetration for this profile is ~10 meters, so the total thickness of these wave package is unknown. These features are much longer than most sandwaves reported in the literature (Sheridan and Updike, 1975; Cole, 1991; Cagnoli and Ulrych, 2001; Douillet et al., 2013, others). However, as discussed above for the dimension of the trough on the western rim profile, such wavelengths have been reported at the Table Rock Complex in Oregon (Brand and Clarke, 2009, 2012). Although outcrops at Rattlesnake Crater are sparse, anti-dune structures are present in the upper units of the tuff ring (Valentine, 2012). The presence of anti-dunes, typically interpreted as the result of highly energetic deposition, lends further strength to the hypothesis that the reflectors seen in the GPR data may be similar in origin to those at Table Rock.

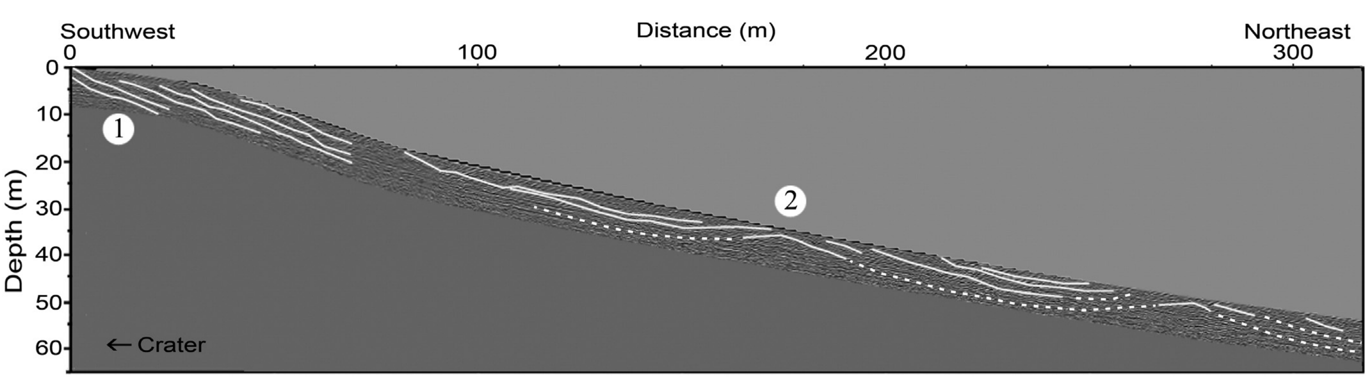

Fig. 7. Profile 2–250 MHz profile over a northeastern section of the tuff ring. GPR "picks" on the eastern side of the tuff ring (see Fig. 1 for location). The profile shows the data corrected for topography and time converted to depth. With topographic correction, reflectors become difficult to make out at this scale, so picks on semi-continuous returns are illustrated for ease of interpretation (solid white lines). Dashed lines indicate hypothesized continuity of reflecting horizons. Numbers 1and 2 mark features discussed in text.

Comparison of GPR data to exposures of dune and sandwave structures documented at other tuff rings could be a valuable tool for studying the eruption dynamics of late-stage phreato-magmatic activity at locations with no cross-sectional tuff ring exposures.

Discussion

Rattlesnake Crater is elongate in a NW–SE direction, the primary orientation of fractures in the area. Nearly all other phreatomagmatic eruption sites in the eastern part of the SFVF also appear to be oriented in this direction. Locally, there are also significant numbers of non-phreatomagmatic volcanic features that have multiple vents or that are elongate in this orientation, such as The Sproul, near Merriam Crater (Ho, 2014). The highest-amplitude magnetic anomalies within Rattlesnake Crater and the vents on Rattlesnake Hill are co-linear and NW-SE trending (Figs. 3 and 4). Based on these observations, we suggest that underlying structural control was responsible for creating aligned features associated with Rattlesnake Crater, and may have aided the flow of groundwater to drive the phreatomagmatic eruption. The relatively impermeable country rock is highly fractured in the eastern part of the SFVF (Gettings and Bultman, 2005), and these fractures can hold significant quantities of water (Montgomery and Harshbarger, 1992; Morgan et al., 2004). It seems logical that phreatomagmatic activity in the SFVF might be triggered by the interaction of magma with these water-filled fractures (e.g. Lorenz, 2003).

Outcrop studies (Valentine and White, 2012; Lefebvre et al., 2013; Delpit et al., 2014) indicate significant local variations in ash/lithic ratios, grainsize, and bedding characteristics; and the occurrence of steeply-dipping contacts are commonplace within diatremes. Diatremes exhibiting zones with highly variable internal properties have also been documented by cores (Brown et al., 2009), physical blast experiments (Graettinger et al., 2014) and geophysical modeling (Blaikie et al., 2014). We interpret the zones of variable density and magnetic properties required to model Rattlesnake Crater gravity and magnetic data in terms of these observations. Modeling of our geophysical data (Fig. 5) suggests that the outermost areas of the diatreme carry the lowest magnetization, yet still have significant apparent magnetic susceptibility contrast with the surrounding, undisturbed country rock. This result is consistent with diatreme deposits containing a relatively low proportion of ash and related juvenile material, and possibly containing blocks, or megablocks of country rock and reworked material emplaced at low temperatures (Delpit et al., 2014). Studies of exposed diatremes show zones along the outer portion can be very rich in wall-rock material (Lefebvre et al., 2013). Diatreme Zone 1 carries higher magnetization than zone 2 in both Models 1 and 2 (Fig. 5). This higher magnetization is likely due to a higher proportion of basaltic fragments in this part of the diatreme. The zones of varying susceptibility within the central part of the diatreme (i.e. Zone 1 and 2) may be a result of a migrating vent within the crater (e.g. Kurszlaukis and Fulop, 2013), or represent a change in eruption dynamics over time.

Diatreme Zone 2 has a density that is consistent with recycled pyroclastic material, but it carries much higher magnetization than expected for such a deposit. The apparent magnetic susceptibility is unlikely to be produced by randomly oriented basalt fragments emplaced at low temperatures, as might be the case in Diatreme Zone 3, because these fragments would have randomly oriented vectors of remnant magnetization. Instead, the high magnetization suggests Diatreme Zone 2 is uniformly magnetized. Its low density and high magnetization are consistent with hot emplacement of non-bedded pyroclastic zones within the diatreme, such as those interpreted to be formed by late-stage intra-diatreme fragmentation (Delpit et al., 2014). The asymmetry of density and susceptibility within the diatreme is also consistent with random explosion depths and/or multiple shallow explosions suggested at other maar–diatremes (Valentine and White, 2012; Blaikie et al., 2014). (Brown et al., 2009; Blaikie et al., 2014; Graettinger et al., 2014).

GPR data reveal possible on-lap features on the lower walls of the crater (Fig. 6, Feature 5), suggesting multiple episodes of phreatomagmatic activity within the crater. GPR data also suggests that the irregular shape of the tuff ring may in part result from faulting on the western side of the ring. We cannot say if the hypothesized faults developed during the eruptive phase of the maar or later, but the uppermost units on Profile 1 (Fig. 6, feature 2) indicate failure occurred before eruptive activity ceased. The geometry and wavelengths of the pyroclastic units revealed in the GPR data (Figs. 6 and 7) suggest that at least some of the eruptive activity at Rattlesnake Crater was highly energetic. Pyroclastic material deposited under high-energy conditions in thick deposits could create the proper conditions to maintain elevated temperature long enough to acquire relatively high TRM, which accounts for the positive magnetic signature of the tuff ring (Figs. 3 & 4, Feature E). We suggest that this high emplacement temperature is consistent with intra-diatreme fragmentation (diatreme Zone 3), following emplacement of diatreme Zones 1 and 2.

The highest amplitude gravity and magnetic anomalies in the crater are related to the dense magnetized body in the center of the crater (Fig. 5, Coherent Body A), which we interpret as a dike intrusion, with a horizontal component that is either a lava flow or a shallow sill located at a depth of 30–40 m beneath the present surface. There are several examples in the exposed diatremes of the nearby Hopi Buttes volcanic field of significant basaltic intrusions emplaced after phreatomagmatic activity ceased (e.g.White, 1991), and late-stage lava ponding is a feature that has been observed at other maars (e.g. Risso et al., 2008). Body B on the right side the diatreme (Fig. 5) could be an intrusion emplaced in a similar manner to Body A, or it could be comprised of spatter internally deposited within a diatreme, as described by (Lefebvre et al., 2012) at Castle Butte South. In that case, spatter deposits were interpreted as the result of pulsating, weak, hot fragmentation (Lefebvre et al., 2012). While most of our geophysical data suggest an energetic eruptive history, spatter deposits could have developed during the transition from phreatomagmatic activity to cone building.

A Brunes-age magnetic orientation and the presence of ash from Sunset crater establishes an age of 900–780,000 B.P. for Rattlesnake Crater. The presence of well-developed weathering horizons in the GPR data suggest Rattlesnake Crater erupted a significant period of time before the Sunset Crater eruption 900 years ago. The relative timing of the formation of the crater and the scoria cone is inconclusive. Deposits from Rattlesnake Hill do overlap the crater and tuff ring in some places. But there is also magnetic evidence that suggest a lava flow from Rattlesnake Hill is covered by material from the tuff ring (Figs. 3 and 4, Feature C). It is not clear if the lava was buried through primary deposition or through the gravitational deformation of the tuff ring through remobilization of pyroclastic sediments over time. Additionally, the presence of a possible unconformity within the tuff outcrop containing basaltic bombs (Valentine, 2012) may also indicate the crater and cone were active concurrently. In any case, it is clear from the geophysical data and their interpretation that Rattlesnake Crater did not form from a simple explosion, but instead was shaped by a series of events including energetic surges, vent migration, dike emplacement, and lava flows.

Conclusions

Gravity and magnetic data provide a basis for modeling the subsurface geometry of the diatreme associated with Rattlesnake Crater. While forward models can have significant uncertainty, the comparison of two models, each developed from both magnetic and gravity data, helps to illustrate the overall concepts required to achieve a good fit to our geophysical data. The gravity and magnetic anomalies indicate the diatreme is not uniform, but instead comprises zones of variable density and magnetization. These zones indicate variable ratios of country rock and juvenile material in the diatreme, shifting vent location through time, and the presence of dense magnetized bodies within the diatreme.

The presence of low density, highly magnetized zones within the diatreme are consistent with massive, unbedded pyroclastic deposits produced by intra-diatreme fragmentation. Approximately 5% of the diatreme, by volume, consists of dense, highly magnetized rock that is interpreted as a late-stage basalt intrusion and/or possible lava flow, on the crater floor or a shallow sill within the upper deposits of the diatreme.

The elongate NW–SE orientation of the crater is mirrored by magnetic anomalies on the crater floor, which are also co-linear with mapped basaltic vents on Rattlesnake Hill. These observations are consistent with structural control on the vent, and the possibility that the phreatomagmatic explosions were driven by the interaction of a magma dike with groundwater contained in fractures of the same orientation. While not commonly observed at phreatomagmatic volcanoes, GPR data reveal the presence of long-wavelength features, complimented by anti-dunes in outcrop, to suggest Rattlesnake Crater experienced an episode of unusually energetic eruptive activity at some point in its formation.

Acknowledgments

This study was partially funded by a Geological Society of America Student Research Grant. This project was truly a team effort and the authors wish to thank Judy McIlrath, Aleeza (Harburger) Wilkins, Nate Nushart, Alex Farrell, Henok Kiflu, Christine Downs, Mary Njoroge, Kyra Rookey, and Karl Wagner for their assistance. We would also like to thank Michael Ort and Greg Valentine for their helpful insights on phreatomagmatic volcanism in the SFVF, as well as James White and Bruno Cagnoli whose thoughtful reviews greatly improved this manuscript.

References

Aranda-Gómez, J.J., Luhr, J.F., Housh, T.B., Connor, C.B., Becker, T., Henry, C.D., 2003. Synextensional Pliocene–Pleistocene eruptive activity in the Camargo volcanic field, Chihuahua, México. Geol. Soc. Am. Bull. 115 (3), 298–313.

Blaikie, T.N., Ailleres, L., Cas, R.A.F., Betts, P.G., 2012. Three-dimensional potential field modelling of a multi-vent maar–diatreme — the Lake Coragulac maar, Newer Volcanics Province, south-eastern Australia. J. Volcanol. Geotherm. Res. 235–236, 70–83.

Blaikie, T.N., Ailleres, L., Betts, P.G., Cas, R.A.F., 2014. A geophysical comparison of the diatremes of simple and complex maar volcanoes, Newer Volcanics Province, south-eastern Australia. J. Volcanol. Geotherm. Res. 276, 64–81.

Bolós, X., Barde-Cabusson, S., Pedrazzi, D., Martí, J., Casas, A., Himi, M., Lovera, R., 2012. Investigation of the inner structure of La Crosa de Sant Dalmai maar (Catalan Volcanic Zone, Spain). J. Volcanol. Geotherm. Res. 247–248, 37–48.

Brand, B.D., Clarke, A.B., 2009. The architecture, eruptive history, and evolution of the Table Rock Complex, Oregon: from a Surtseyan to an energetic maar eruption. J. Volcanol. Geotherm. Res. 180 (2), 203–224.

Brand, B.D., Clarke, A.B., 2012. An unusually energetic basaltic phreatomagmatic eruption: using deposit characteristics to constrain dilute pyroclastic density current dynamics. J. Volcanol. Geotherm. Res. 243–244, 81–90.

Brown, R., Tait, M., Field, M., Sparks, R., 2009. Geology of a complex kimberlite pipe (K2 pipe, Venetia Mine, South Africa): insights into conduit processes during explosive ultrabasic eruptions. Bull. Volcanol. 71 (1), 95–112.

Cagnoli, B., Ulrych, T., 2001. Ground penetrating radar images of unexposed climbing dune-forms in the Ubehebe hydrovolcanic field (Death Valley, California). J. Volcanol. Geotherm. Res. 109 (4), 279–298.

Cassidy, J., Locke, C.A., 2010. The Auckland volcanic field, New Zealand: Geophysical evidence for structural and spatio-temporal relationships. J. Volcanol. Geotherm. Res. 195 (2), 127–137.

Cassidy, J., France, S.J., Locke, C.A., 2007. Gravity and magnetic investigation of maar volcanoes, Auckland volcanic field, New Zealand. J. Volcanol. Geotherm. Res. 159 (1-3), 153–163.

Chester, D.K., Degg, M., Duncan, A.M., Guest, J., 2000. The increasing exposure of cities to the effects of volcanic eruptions: a global survey. Glob. Environ. Chang. Part B Environ. Hazards 2 (3), 89–103.

Chough, S.K., S, Y.K., 1990. Depositional mechanics and sequences of base surges, Songksan tuff ring, Cheju Island, Korea. Sedimentology 37, 1115–1135.

Clement, B.M., Connor, C.B., Graper, G., 1993. Paleomagnetic estimate of the emplacement temperature of the long-runout Nevado de Colima volcanic debris avalanche deposit, Mexico. Earth Planet. Sci. Lett. 120 (3), 499–510.

Cole, P., 1991. Migration direction of sand-wave structures in pyroclastic-surge deposits: implications for depositional processes. Geology 19 (11), 1108–1111.

Condit, C.D., Crumpler, L., Aubele, J.C., Elston, W.E., 1989. Patterns of volcanism along the southern margin of the Colorado Plateau: the Springerville field. J. Geophys. Res. Solid Earth 94 (B6), 7975–7986 (1978–2012).

Conway, F.M., Ferrill, D.A., Hall, C.M., Morris, A.P., Stamatakos, J.A., Connor, C.B., Halliday, A.N., Condit, C., 1997. Timing of basaltic volcanism along the Mesa Butte Fault in the San Francisco Volcanic Field, Arizona, from 40Ar/39Ar dates: implications for longevity of cinder cone alignments. J. Geophys. Res. 102 (B1), 815.

Courtland, L., Kruse, S.E., Connor, C.B., Connor, L., Savov, I., Martin, K., 2012. GPR investigation of tephra fallout, Cerro Negro volcano, Nicaragua: a method for constraining parameters used in tephra sedimentation models. Bull. Volcanol. 74 (6), 1409–1424.

Courtland, L., Kruse, S., Connor, C., 2013. Violent Strombolian or not? Using ground-penetrating radar to distinguish deposits of low-and high-energy scoria cone eruptions. Bull. Volcanol. 75 (12), 1–13.

Davis, J., Annan, A., 1989. Ground-penetrating radar for high resolution mapping of soil and rock stratigraphy. Geophys. Prospect. 37 (5), 531–551.

Delaney, P.T., Gartner, A.E., 1997. Physical processes of shallow mafic dike emplacement near the San Rafael Swell, Utah. Geol. Soc. Am. Bull. 109 (9), 1177–1192.

Delpit, S., Ross, P.-S., Hearn Jr., B.C., 2014. Deep-bedded ultramafic diatremes in the Missouri River Breaks volcanic field, Montana, USA: 1 km of syn-eruptive subsidence. Bull. Volcanol. 76 (7), 1–22.

Douillet, G.A., Pacheco, D.A., Kueppers, U., Letort, J., Tsang-Hin-Sun, E., Bustillos, J., Hall, M., Ramon, P., Dingwell, D.B., 2013. Dune bedforms produced by dilute pyroclastic density currents from the August 2006 eruption of Tungurahua volcano, Ecuador. Bull. Volcanol. 75 (11), 762.

Dunlop, D., 1989. Viscous remanent magnetization (VRM) and viscous remagnetization. Encyclopedia of Solid Earth Geophysicspp. 1297–1303.

Fontana, G., Mac Niocaill, C., Brown, R.J., Sparks, R.S.J., Field, M., 2011. Emplacement temperatures of pyroclastic and volcaniclastic deposits in kimberlite pipes in southern Africa. Bull. Volcanol. 73 (8), 1063–1083.

George, O.A., McIlrath, J., Farrell, A., Gallant, E., Tavarez, S., Marshall, A., McNiff, C., Njoroge, M., Wilson, J., Connor, C., 2015. High-resolution ground-based magnetic survey of a buried volcano: anomaly B, Amargosa Desert, NV. Stat. Volcanol. 1 (1), 3.

Gettings, M.E., Bultman, M.W., 2005. A predictive penetrative fracture mapping method from regional potential field and geologic datasets, southwest Colorado Plateau, USA. Earth Planets Space 57 (8), 701.

Gomez, C., Lavigne, F., Lespinasse, N., Hadmoko, D.S., Wassmer, P., 2008. Longitudinal structure of pyroclastic-flow deposits, revealed by GPR survey, at Merapi Volcano, Java, Indonesia. J. Volcanol. Geotherm. Res. 176 (4), 439–447.

Gómez-Ortiz, D., Martín-Velázquez, S., Martín-Crespo, T., Márquez, A., Lillo, J., López, I., Carreño, F., 2006. Characterization of volcanic materials using ground penetrating radar: a case study at Teide volcano (Canary Islands, Spain). J. Appl. Geophys. 59 (1), 63–78.

Graettinger, A., Valentine, G., Sonder, I., Ross, P.S., White, J., Taddeucci, J., 2014. Maar-diatreme geometry and deposits: subsurface blast experiments with variable explosion depth. Geochem. Geophys. Geosyst. 15 (3), 740–764.

Guffanti, M., Clynne, M.A., Smith, J.G., Muffler, L., Bullen, T.D., 1990. Late Cenozoic volcanism, subduction, and extension in the Lassen region of California, southern Cascade Range. J. Geophys. Res. Solid Earth 95 (B12), 19453–19464 (1978–2012).

Guha, S., Kruse, S.E., Wright, E., Kruse, U., 2005. Spectral analysis of ground penetrating radar response to thin sedimentary layers. Geophys. Res. Lett. 32 (23).

Harburger, A.M., 2014. Probabilistic Modeling of Lava Flows: A Hazard Assessment for the San Francisco Volcanic Field. University of South Florida, Arizona.

Hashimoto, T., Hurst, T., Suzuki, A., Mogi, T., Yamaya, Y., Tamura, M., 2008. The role of Thermal Viscous Remanent Magnetisation (TVRM) in magnetic changes associated with volcanic eruptions: insights from the 2000 eruption of Mt Usu, Japan. J. Volcanol. Geotherm. Res. 176 (4), 610–616.

Ho, K.T., 2014. Identifying Vent Location and Eruptive Behavior at The Sproul Crater, San Francisco Vlocanic Field REU, 2014 GSA Annual Meeting in Vancouver. British Columbia.

Hoffmann, J.P., Bills, D., Phillips, J., Halford, K., 2006. Geologic, Hydrologic, and Chemical Data from the C Aquifer near Leupp, Arizona. US Department of the Interior, US Geological Survey.

Jarvis, A., Reuter, H.I., Nelson, A., Guevara, E., 2008. Hole-filled SRTM for the globe Version 4 (available from the CGIAR-CSI SRTM 90 m, Database (http://srtm.csi.cgiar.org)).

Kiyosugi, K., Connor, C., Zhao, D., Connor, L., Tanaka, K., 2010. Relationships between volcano distribution, crustal structure, and P-wave tomography: an example from the Abu Monogenetic Volcano Group, SW Japan. Bull. Volcanol. 72 (3), 331–340.

Kruse, S., Mora-Amador, R., Ramírez, C., Alvarado, G.E., 2010. Ground Penetrating Radar Imaging of Tephra Stratigraphy on Poás and Irazú Volcanoes. 43. Revista Geológica de América Central, Costa Rica, pp. 119–136.

Kurszlaukis, S., Fulop, A., 2013. Factors controlling the internal facies architecture of maar–diatreme volcanoes. Bull. Volcanol. 75 (11), 1–12.

Lefebvre, N., White, J., Kjarsgaard, B., 2012. Spatter-dike reveals subterranean magma diversions: consequences for small multivent basaltic eruptions. Geology 40 (5), 423–426.

Lefebvre, N., White, J., Kjarsgaard, B., 2013. Unbedded diatreme deposits reveal maar–diatreme-forming eruptive processes: Standing Rocks West, Hopi Buttes, Navajo Nation, USA. Bull. Volcanol. 75 (8), 1–17.

López Loera, H., Aranda-Gómez, J.J., Arzate, J.A., Molina-Garza, R.S., 2008. Geophysical surveys of the Joya Honda maar (México) and surroundings; volcanic implications. J. Volcanol. Geotherm. Res. 170 (3-4), 135–152.

Lorenz, V., 2003. Maar–diatreme volcanoes, their formation, and their setting in hard-rock or soft-rock environments. Geolines 15, 72–83.

Lorenz, V., Kurszlaukis, S., 2007. Root zone processes in the phreatomagmatic pipe emplacement model and consequences for the evolution of maar–diatreme volcanoes. J. Volcanol. Geotherm. Res. 159 (1), 4–32.

Mandeville, C.W., Carey, S., Sigurdsson, H., King, J., 1994. Paleomagnetic evidence for high-temperature emplacement of the 1883 subaqueous pyroclastic flows from Krakatau Volcano, Indonesia. J. Geophys. Res. Solid Earth 99 (B5), 9487–9504 (1978–2012).

McPhie, J., Walker, G.P., Christiansen, R.L., 1990. Phreatomagmatic and phreatic fall and surge deposits from explosions at Kilauea volcano, Hawaii, 1790 AD: Keanakakoi Ash Member. Bull. Volcanol. 52 (5), 334–354.
Montgomery, E., Harshbarger, J., 1992. Arizona hydrogeology and water supply. J. Appl. Hydrol. 1 (1), 25–40.
Morales, J., Alva-Valdivia, L.M., Goguitchaichvili, A., Urrutia-Fucugauchi, J., 2006. Cooling rate corrected paleointensities from the Xitle lava flow: evaluation of within-site scatter for single spot-reading cooling units. Earth Planets Space 58 (10), 1341–1347.
Morgan, P., Sass, J.H., Duffield, W., Fleger, T., Fry, B.N. and Peters, L., 2004. Geothermal resource evaluation program of the Eastern San Francisco Volcanic Field, Arizona. Unpublished final report to the Department of Energy, Project GRED II, Agreement# DE-FC04-2002AL68298, Department of Geology, Northern Arizona University: 40.
Mrlina, J., Kämpf, H., Kroner, C., Mingram, J., Stebich, M., Brauer, A., Geissler, W.H., Kallmeyer, J., Matthes, H., Seidl, M., 2009. Discovery of the first Quaternary maar in the Bohemian Massif, Central Europe, based on combined geophysical and geological surveys. J. Volcanol. Geotherm. Res. 182 (1-2), 97–112.
Nemeth, K., White, J.D., Reay, A., Martin, U., 2003. Compositional variation during monogenetic volcano growth and its implications for magma supply to continental volcanic fields. J. Geol. Soc. 160 (4), 523–530.
Ort, M.H., Carrasco-Núñez, G., 2009. Lateral vent migration during phreatomagmatic and magmatic eruptions at Tecuitlapa Maar, east-central Mexico. J. Volcanol. Geotherm. Res. 181 (1), 67–77.
Ort, M.H., Elson, M.D., Anderson, K.C., Duffield, W.A., Hooten, J.A., Champion, D.E., Waring, G., 2008. Effects of scoria-cone eruptions upon nearby human communities. Geol. Soc. Am. Bull. 120 (3-4), 476–486.
Popowski, T., Connard, G., French, R., 2009. GMSYS Profile Modeling: Gravity & Magnetic Modeling Software for Oasis Montaj–User Guide v. 4.1. Geosoft Inc., Torronto, Ontario.
Priest, S.S., Duffield, W.A., Malis-Clark, K., Hendley II, J.W., Stauffer, P.H., 2001. The San Francisco Volcanic Field. Arizona, US Geological Survey.
Re, G., White, J., Ort, M., 2015. Dikes, sills, and stress-regime evolution during emplacement of the Jagged Rocks Complex, Hopi Buttes Volcanic Field, Navajo Nation, USA. J. Volcanol. Geotherm. Res. 295, 65–79.
Riggs, N., Duffield, W., 2008. Record of complex scoria cone eruptive activity at Red Mountain, Arizona, USA, and implications for monogenetic mafic volcanoes. J. Volcanol. Geotherm. Res. 178 (4), 763–776.
Risso, C., Németh, K., Combina, A.M., Nullo, F., Drosina, M., 2008. The role of phreatomagmatism in a Plio-Pleistocene high-density scoria cone field: Llancanelo Volcanic Field (Mendoza), Argentina. J. Volcanol. Geotherm. Res. 169 (1), 61–86.
Roddy, D., 1978. Pre-impact conditions and cratering processes at Meteor Crater, Arizona, a typical bowl-shaped crater. Lunar and Planetary Science Conference Proceedings, pp. 3891–3930.
Russell, J.K., Stasiuk, M.V., 1997. Characterization of volcanic deposits with ground-penetrating radar. Bull. Volcanol. 58 (7), 515–527.
Schulz, R., Buness, H., Gabriel, G., Pucher, R., Rolf, C., Wiederhold, H., Wonik, T., 2005. Detailed investigation of preserved maar structures by combined geophysical surveys. Bull. Volcanol. 68 (2), 95–106.
Sheridan, M.F., Updike, R.G., 1975. Sugarloaf Mountain Tephra—a Pleistocene rhyolitic deposit of base-surge origin in northern Arizona. Geol. Soc. Am. Bull. 86 (4), 571–581.
Skácelová, Z., Rapprich, V., Valenta, J., Hartvich, F., Šrámek, J., Radoň, M., Gaždová, R., Nováková, L., Kolínský, P., Pécskay, Z., 2012. Geophysical research on structure of partly eroded maar volcanoes: Miocene Hnojnice and Oligocene Rychnov volcanoes (northern Czech Republic). J. Geosci. 333–345.
Sohn, Y.K., Chough, S.K., 1989. Depositional processes of the Suwolbong tuff ring, Cheju Island (Korea). Sedimentology 36 (5), 837–855.
Sohn, Y.K., Park, K.H., 2005. Composite tuff ring/cone complexes in Jeju Island, Korea: possible consequences of substrate collapse and vent migration. J. Volcanol. Geotherm. Res. 141 (1-2), 157–175.
Sulpizio, R., Zanella, E., Macías, J.L., 2008. Deposition temperature of some PDC deposits from the 1982 eruption of El Chichon volcano (Chiapas, Mexico) inferred from rock-magnetic data. J. Volcanol. Geotherm. Res. 175 (4), 494–500.
Tanaka, K.L., Shoemaker, E.M., Ulrich, G.E., Wolfe, E.W., 1986. Migration of volcanism in the San Francisco volcanic field, Arizona. Geol. Soc. Am. Bull. 97 (2), 129–141.
Valentine, G.A., 2012. Shallow plumbing systems for small-volume basaltic volcanoes, 2: Evidence from crustal xenoliths at scoria cones and maars. J. Volcanol. Geotherm. Res. 223, 47–63.
Valentine, G.A., White, J.D.L., 2012. Revised conceptual model for maar–diatremes: subsurface processes, energetics, and eruptive products. Geology 40 (12), 1111–1114.
van Kooten, G.K., Buseck, P.R., 1978. Interpretation of olivine zoning: study of a maar from the San Francisco volcanic field, Arizona. Geol. Soc. Am. Bull. 89 (5), 744–754.
van Otterloo, J., Cas, R.A.F., 2013. Reconstructing the eruption magnitude and energy budgets for the pre-historic eruption of the monogenetic ~5 ka Mt. Gambier Volcanic Complex, south-eastern Australia. Bull. Volcanol. 75 (12), 1–18.
Vazquez, J.A., Ort, M.H., 2006. Facies variation of eruption units produced by the passage of single pyroclastic surge currents, Hopi Buttes volcanic field, USA. J. Volcanol. Geotherm. Res. 154 (3-4), 222–236.
White, J.D., 1991. Maar–diatreme phreatomagmatism at Hopi Buttes, Navajo Nation (Arizona), USA. Bull. Volcanol. 53 (4), 239–258.
White, J.D.L., Ross, P.S., 2011. Maar–diatreme volcanoes: a review. J. Volcanol. Geotherm. Res. 201 (1), 1–29.
White, J., Karakhanian, A., Connor, C., Connor, L., Hughes, J., Malservisi, R., Wetmore, P., 2015. Coupling geophysical investigation with hydrothermal modeling to constrain the enthalpy classification of a potential geothermal resource. J. Volcanol. Geotherm. Res. 298, 59–70.
Wohletz, K.H., Sheridan, M.F., 1983. Hydrovolcanic explosions; II, Evolution of basaltic tuff rings and tuff cones. Am. J. Sci. 283 (5), 385–413.
Zimmer, B.W., Riggs, N.R., Carrasco-Núñez, G., 2010. Evolution of tuff ring-dome complex: the case study of Cerro Pinto, eastern Trans-Mexican Volcanic Belt. Bull. Volcanol. 72 (10), 1223–1240.